HHS Public Access

Author manuscript

J Neurosci Methods. Author manuscript; available in PMC 2019 November 01.

Published in final edited form as:

J Neurosci Methods. 2018 November 01; 309: 121–131. doi:10.1016/j.jneumeth.2018.08.018.

Spatially adaptive unsupervised multispectral nonlocal filtering for improved cerebral blood flow mapping using arterial spin labeling magnetic resonance imaging

Mustapha Bouhrara[*], **Diana Y. Lee**[#], **Abinand C. Rejimon**[#], **Christopher M. Bergeron**, and **Richard G. Spencer**

Laboratory of Clinical Investigation, National Institute on Aging, NIH, Baltimore, Maryland, USA.

[#] These authors contributed equally to this work.

Abstract

Background: Cerebral blood flow (CBF) is an emerging biomarker for normal aging and neurodegenerative diseases. Arterial spin labeling (ASL) perfusion MRI permits noninvasive quantification of CBF. However, high-quality mapping of CBF from ASL imaging is challenging, largely due to noise.

New Method: We demonstrate the ability of the recently introduced nonlocal estimation of multispectral magnitudes (NESMA) filter to greatly improve determination of CBF estimates from ASL imaging data. We evaluated the results of NESMA-ASL for CBF mapping from data obtained on human brain (n=10) across a wide age range (21–74 years) using a standard clinical protocol. Results were compared to those obtained from unfiltered images or filtered images using conventional and advanced filters. Quantitative analyses for different spatial image resolutions and signal-to-noise ratios, SNRs, were also conducted.

Results: Our results demonstrate the potential of NESMA-ASL to permit high-quality high-resolution CBF mapping. NESMA-ASL substantially reduces random variation in derived CBF estimates while preserving edges and small structures, with minimal bias and dispersion in derived CBF estimates.

Comparison with Existing Methods: NESMA-ASL outperforms all evaluated filters in terms of noise reduction and detail preservation. Further, unlike other filters, NESMA-ASL is straightforward to implement requiring only one user-defined parameter, which is relatively insensitive to SNR or local image structure.

Conclusions: *In-vivo* estimation of CBF in the human brain from ASL imaging data was markedly improved through use of the NESMA-ASL filter. The use of NESMA-ASL may

[*]Address correspondence to: Mustapha Bouhrara, PhD., National Institutes of Health (NIH), National Institute on Aging (NIA), Intramural Research Program, BRC 04B-117, 251 Bayview Boulevard, Baltimore, MD 21224, USA. Tel: 410-558-8541, bouhraram@mail.nih.gov.

contribute significantly to the goal of high-quality high-resolution CBF mapping within a clinically feasible acquisition time.

Keywords

CBF; ASL; Filtering

1 INTRODUCTION

Cerebral blood flow (CBF), measured using arterial spin labeling (ASL), is a critical physiological descriptor of brain health in normative aging, Alzheimer's disease, and other neurodegenerative conditions (Petcharunpaisan et al., 2010; Williams et al., 1992). CBF quantification from single- phase ASL imaging generally requires a set of three images: control image, labeled image acquired after magnetic labeling the blood in the feeding vessels, and proton density (PD) image (Alsop et al., 2015). The difference between the two former images is used to map the ASL signal, reflecting the amount of labeled blood that has been delivered to the imaging region, while the PD image is used to scale the ASL signal to absolute CBF units.

ASL is a subtraction technique, with relatively small signal differences between the control and labeled images (Alsop et al., 2015). This places extreme demands on the signal-to-noise-ratio (SNR) for image acquisition. Signal averaging is often used to improve SNR but comes at the expense of increased acquisition time or acquisition of limited resolution images. However, rapid whole-brain coverage is needed for clinical applications, especially those involving patients with limited ability to remain stationary for the lengthy duration of magnetic resonance imaging (MRI) studies (Pollock et al., 2009). In addition, high-resolution (HR) mapping is required to define small regional CBF changes, as could be the case in multiple sclerosis, and to reduce partial volume effects (Zhao et al., 2017).

Previous work has sought to improve CBF determination through application of conventional and advanced noise reduction filters during post-processing (Spann et al., 2017; Tan et al., 2009; Wells et al., 2010; Zhu et al., 2018). These include Gaussian averaging (GA) (Wells et al., 2010), adaptive Wiener filtering (Spann et al., 2017; Wells et al., 2010), total generalized variation (Spann et al., 2017), anisotropic diffusion (Wells et al., 2010), nonlocal means (Liang et al., 2015; Petr et al., 2010), and wavelet-based filters (Bibic et al., 2010). These filters are effective but suffer from a high level of complexity and the requirement for supervised implementation for optimal performance; that is, performance can be properly tuned in test cases, but is much more challenging in actual practice. In fact, the required tuning parameters depend on the characteristics of the analyzed dataset (*e.g.* SNR) adding further complexity in implementation.

In contrast, we have developed and implemented a new filter, denoted the *Nonlocal Estimation of multi-Spectral Magnitudes* (NESMA), that is conceptually simple, easy to apply, and, given its spatially adaptive capability, may be implemented in an essentially unsupervised fashion. We have shown that NESMA, while simple, demonstrates excellent noise reduction and quality of image feature preservation (Bouhrara et al., 2017a; Maring. et al., 2017). The NESMA filter is nonlocal (NL), meaning that it incorporates information

from non-adjacent voxels, and multispectral (MS), meaning that it incorporates image intensities from different acquisition modalities or experimental parameter values. Specifically, NESMA restores the intensity of an index voxel based on averaged voxel intensities of M selected similar voxels. In the case of ASL datasets, the M selected voxels can be defined as those that exhibit signal intensities similar to that of the index voxel within the control, labeled, and PD images, with the criterion for similarity to be defined below. NESMA filtering is very fast, rendering it suitable for routine use and analysis of large datasets, and requires only one user-defined parameter that is straightforward to define and has an optimal value that is relatively insensitive to image SNR.

The main objective of this study is to evaluate the performance of the NESMA-ASL filter for CBF determination from single-phase ASL imaging of the human brain, and to compare the results to those obtained from unfiltered images and from filtered images using conventional and advanced filters. The plan of the paper is as follows. First, we describe and detail the implementation of the NESMA-ASL filter. We then present numerical and *in-vivo* results for the evaluation of NESMA-ASL and the other filters. Next, we present CBF results obtained from human brain, with and without NESMA-ASL filtering, acquired with different image resolutions, SNRs, and in subjects of different ages. Finally, we discuss the performance, advantages, and limitations of NESMA-ASL and the other filters evaluated.

2 METHODS

2.1 The NESMA-ASL image filtering algorithm

The underlying idea of quantitative noise reduction filters is to replace the observed intensity of an index voxel i with an improved unbiased estimate of its underlying amplitude. This requires additional intensity information to be obtained from voxels that are selected as being likely to come from similar tissue. The earliest filters, including the boxcar and Gaussian averaging filters, incorporate intensities from adjacent voxels. This leads to loss of image detail. Multispectral nonlocal filters, including NESMA, restore the amplitude of an index voxel by incorporating the intensities of M voxels with similar multispectral signal patterns, that is, intensities from different acquisition modalities or experimental parameter values (Bouhrara et al., 2017a; Maring. et al., 2017). The CBF map is generally derived from three different images, namely, the control image, S_C, the labeled image, S_L, and the proton density (PD) image, S_{PD}, so that we may consider these image sets as multispectral. The estimates $\hat{A}_C(i)$, $\hat{A}_L(i)$, and $\hat{A}_{PD}(i)$ of the true amplitudes in index voxel i are given by:

$$\begin{aligned}\hat{A}_C(i) &= M^{-1}\sum_j^M S_C(j), \\ \hat{A}_L(i) &= M^{-1}\sum_j^M S_L(j), \\ \hat{A}_{PD}(i) &= M^{-1}\sum_j^M S_{PD}(j).\end{aligned} \qquad [1]$$

The similarity between two voxels i and j across the three images of the multispectral set is calculated using the relative Euclidean distance, RED, given by:

$$\mathrm{RED}\ (i,j) = 100 \times \frac{\sqrt{\left(S_C(i) - S_C(j)\right)^2 + \left(S_L(i) - S_L(j)\right)^2 + \left(S_{PD}(i) - S_{PD}(j)\right)^2}}{\sqrt{S_C^2(i) + S_L^2(i) + S_{PD}^2(i)}}. \quad [2]$$

The point of this normalization is to permit the incorporation of more or fewer voxels, depending upon the local structure and intensity variation within the image. RED is calculated between the index voxel, *i*, and every other voxel, *j*, within a large search window, *R*, centered on *i*. The size of the window *R* must be sufficiently large to ensure inclusion of an adequate number of similar voxels, and sufficiently restricted to ensure that the transmission and reception *B1* fields and noise standard deviation (SD) are approximately constant within the window. Voxels exhibiting RED < 5% are considered as being similar to the index voxel. This results in the selection of a subset of *M* voxels designated to be similar to *i* from which $\hat{A}_C(i), \hat{A}_L(i)$, and $\hat{A}_{PD}(i)$ are computed using Eq. 1. In the following, we will refer to this filter as NESMA-ASL.

2.2 CBF mapping

CBF was calculated for each voxel *i* according to (Alsop et al., 2015):

$$\mathrm{CBF}\ (i) = 6000 \times \frac{\lambda \cdot \left(I_C(i) - I_L(i)\right) \cdot exp\left(\mathrm{PLD}\ / T_{1,Blood}\right)}{2\alpha \cdot T_{1,Blood} \cdot I_{PD}(i) \cdot \left(1 - exp(-\tau / T_{1,Blood})\right)} [m\ \mathrm{L}\ /100g/\ \mathrm{min}], \quad [3]$$

where I_C, I_L, and I_{PD} are intensities within the control, labeled, and PD images; these correspond to S_C, S_L and S_{PD} for the unfiltered (*i.e.* original) images, or to $\hat{A}_C, \hat{A}_L$ and $\hat{A}_{PD}$ for the filtered images. Here, λ is the partition coefficient between brain tissue and blood, set to 0.9 mL/g, α is the labeling efficiency with value fixed to 0.85, $T_{1,Blood} = 1.65\ s\ (at\ 3T)$ representing the longitudinal relaxation time of blood, and τ and PLD are the label duration and post labeling delay, respectively. In this work, and PLD were fixed to 1.8 s and 2 s, respectively (*c.f.* "*In-vivo analysis*" section). For more details, see Ref. 3. We note the availability of other signal models for CBF, as well as uncertainties in the appropriate values for the parameters within Eq. [3]. However, our focus here is on the improvement in performance through use of NESMA-ASL-filtered images, which is independent of the specifics of the model or parameters used.

2.3 Simulation analysis

Simulations were conducted to evaluate and compare the performance of NESMA-ASL to a selection of conventional or advanced filters as described below. Noise-free control, labeled, and PD images were constructed to create a reference CBF map. We applied noise reduction filters to images obtained from Subject 2 to create realistic reference noise-free images and a corresponding reference CBF map. Gaussian noise with SD, σ, was then added to create noisy images at two different SNRs of 225, corresponding to typical experimental values (see *In-vivo* analysis section), or 450, corresponding to exceptionally high-quality data for

further illustration. SNR was defined as the mean signal value calculated over large white matter regions from the control image, divided by σ. CBF maps were then derived using Eq. 3 from this dataset after processing using the indicated filters.

As noted above, many advanced filters require optimization through adjustment of tuning parameters; this can have a major impact on the denoising performance. To ensure a fair comparison, tuning parameters were first optimized for each filter, each SNR, and each image (*i.e.* control, labeled and PD). Optimal tuning parameters were considered to be those that maximized the structural similarity index (SSIM) between the reference CBF map and the CBF map derived after filtering (Spann et al., 2017). The SSIM was computed voxel-wise and then averaged over all parenchymal voxels defined through manual segmentation. We used the MATLAB function "ssim" to compute SSIM with radius and regularization factor set to default values. Further, it has been shown that the optimal tuning parameters can differ between slices of the same subject, adding further complexity to the implementation of most advanced filters (Spann et al., 2017). Therefore, analysis was restricted to the middle slice of the generated dataset. The local or nonlocal filters evaluated are:

2.3.1. Local filters: - ***Boxcar averaging (BA) filter***: The size of the local kernel was set to 3 voxels x 3 voxels, with filtering implemented using the MATLAB function "imboxfilt".

- ***Gaussian averaging (GA) filter***: The size of the local kernel was set to 5 voxels x 5 voxels, with filtering implemented using the MATLAB function "imgaussfilt".

- ***Adaptive Wiener (AW) filter*** (Jin et al., 2003; Spann et al., 2017; Wells et al., 2010): The kernel size was set to 5 voxels x 5 voxels, while the noise variance was optimized for each SNR by maximizing the SSIM . Filtering was performed using the MATLAB function "wiener2".

2.3.2. Nonlocal filters: - ***NESMA-ASL***: R was set to 11 voxels x 11 voxels, and voxels with RED < 5% were considered similar to the index voxel.

- ***Anisotropic diffusion (AD) filter*** (Gerig et al., 1992; Perona and Malik, 1990; Wells et al., 2010): Diffusion step time and the number of iterations were set to 0.25 and 5, respectively, while the conduction coefficient K was optimized for each SNR by maximizing the SSIM. Filtering was performed using a MATLAB implementation available at: https://www.mathworks.com/matlabcentral/fileexchange/14995-anisotropic-diffusion--perona---malik.

- ***Nonlocal means (NLM) filter*** (Buades et al., 2005; Liang et al., 2015; Petr et al., 2010): As recommended previously (Buades et al., 2005; Liang et al., 2015; Petr et al., 2010), the size of the search window, R, was set to 11 voxels x 11 voxels and the size of the local patch was set to 3 voxels x 3 voxels. The smoothing parameter, h, was optimized for each SNR by maximizing the SSIM. Filtering was performed using a MATLAB implementation available at: https://www.mathworks.com/matlabcentral/fileexchange/13176-non-local-means-filter.

- ***Block matching 3D (BM3D) filter*** (Dabov et al., 2007): The filter profile was set to "high" (Dabov et al., 2007; Spann et al., 2017), while the noise SD was optimized for each SNR by

maximizing the SSIM. We used the MATLAB implementation available at: http://www.cs.tut.fi/~foi/GCF-BM3D/.

- ***Total generalized variation (TGV) filter*** (Bredies et al., 2010; Spann et al., 2017): The number of iterations was set to 5 while the balancing weights parameters were optimized for each SNR by maximizing the SSIM. We used the following MATLAB implementation: https://www.mathworks.com/matlabcentral/fileexchange/49717-image-denoising-by- total--generalized--variation-via-fft.

For each filter and SNR, we assessed the bias, a measure of accuracy, and the dispersion, a measure of precision, in CBF determination for each index voxel i over $N = 1001$ noiserealizations according to:$\text{bias}(i) = N^{-1}\sum_{n=1}^{N}\left|\mathrm{CBF}_{est,n}(i) - \mathrm{CBF}_{ref}(i)\right|$ and $\text{dispersion}(i) = \sqrt{N^{-1}\sum_{n=1}^{N}\left(\mathrm{CBF}_{est,n}(i) - \mathrm{CBF}_{ref}(i)\right)^2}$ where CBF_{ref} and CBF_{est}correspond to reference and estimated CBF maps, respectively. Representative CBF maps were derived from a single noise realization of each of the two SNRs investigated, before and after filtering. Maps of bias and dispersion in CBF values, as well as their means and SD, calculated over all parenchymal voxels were also derived. All analyses were performed using MATLAB software (MathWorks, Natick, MA, USA) on a 2.4-GHz computer.

2.4. In-vivo analysis

Ten healthy and cognitively intact volunteers (Table 1) were scanned with a 2D pseudo-continuous ASL (pCASL) sequence combined with single-shot echo-planar-imaging acquisition on a 3TPhilips Achieva MRI system (Best, Netherlands), using an 8-channel head coil. The experimental procedures were fully explained to the subjects and written informed consent was obtained prior to participation. All examinations were performed in compliance with the standards established by our local Institutional Review Board (IRB). This comprehensive IRB approval process incorporates all current ethical standards established by the National Institutes of Health for studies of human subjects. For each participant S_C, S_L, and S_{PD} images were acquired at conventional resolution (CR): 2.8 mm x 2.8 mm x 5 mm, with reconstruction to 1.5 mm x 1.5 mm x 5 mm. High resolution (HR) images, acquired with spatial resolution of 1.9 mm x 1.9 mm x 5 mm and reconstructed to 1 mm x 1 mm x 5 mm, were obtained from the brains of 4 participants (Table 1). Other experimental parameters were: TE = 13 ms, TR = 7.5 s, $\tau = 1.8$ s, PLD = 2 s, with incorporation of background suppression. ASL images were acquired with different values for the number of signal averages (NSA) of 3, 5, 10, 20, and 30. The acquisition time for one NSA was~22 s. Four distinct analyses were performed.

Analysis #1: CBF maps derived from unfiltered and filtered ASL images, using each of the filters described above, were compared. Analysis was performed on two CR *in-vivo* datasets obtained from the brain of the 21-year-old and 50-year-old participants with NSA of 30, and results were displayed for two different slices for each participant. Tuning parameters were identical to those used in the simulations with SNR = 225.

Analysis #2: CR and HR CBF maps derived from unfiltered images or from filtered images using the NESMA-ASL filter were compared. Analysis was performed on the CR and HR *in-vivo* NSA = 30 datasets obtained from the brain of the 61-years-old participant, and results were displayed for three different slices. To ensure similar window search volume around the index voxels, the size of R was set to 15 voxels x 15 voxel x 1 voxels for HR images, and to 11 voxels x 11 voxels x 1 voxel for CR images. For both HR and CR, voxels with RED < 5% were considered similar to the index voxel. The SNR values were ~225 and ~160 for CR and HR, respectively.

Analysis #3: This analysis consisted of comparing CBF maps obtained for different NSAs using the HR *in-vivo* dataset from the brain of the 50-year-old participant and using NESMA-ASL filtering. For each NSA, results were displayed for two representative slices before and after the NESMA-ASL filtering. The mean and SD CBF values were also calculated over large white or gray matter regions, defined through manual segmentation, after setting voxels with negative CBF values to zero (Baskerville et al., 2012). For all NSAs, the size of R was set to 15 voxels x 15 voxels x 1 voxel and the RED threshold was again set to < 5%.

Analysis #4: This analysis consisted of comparing CBF maps derived from all participants, representing a wide age range, before and after NESMA-ASL filtering. Analysis was performed on the CR imaging datasets, with results displayed for two representative slices. Moreover, the mean and SD CBF values were calculated in four different white or gray matter regions-of-interest (ROIs) defined through manual segmentation. The ROIs lay within the frontal, parietal, occipital, and temporal lobes. Intensities of voxels with negative CBF values were set to zero.

3. RESULTS

Figure 1 shows simulation results for CBF maps derived from unfiltered and filtered ASL data using different local (*i.e.* BG, BA, and AW) filters and the nonlocal filters described above. Results are shown for both SNRs investigated. It is readily seen that, as expected, all filters substantiallyreduce random variations in derived CBF maps. In addition, the local filters introduce a much greater degree of blurring than do the nonlocal NESMA-ASL, NLM, and TGV filters, especially in regions located between gray and white matter. Furthermore, the bias maps, calculated as described above for each voxel independently, and values for the mean and SD of these bias values, calculated over all parenchymal regions, show that NESMA-ASL, GA, and TGV result in a much smaller degree of bias in derived CBF estimates as compared to the other filters investigated. Moreover, NESMA-ASL shows the greatest precision, that is, lowest dispersion, among all evaluated filters. Finally, at high SNR, all evaluated filters performed well in term of precision, but with clear superiority of NESMA-ASL, GA, and BM3D. The processing times to denoise the entire ASL data set for one noise realization were 0.7 s, 0.3 s, 0.2 s, 0.2 s, 14 s, 0.1 s, 0.1 s, and 0.4, for NESMA-ASL, AD, BA, BG, NLM, AW, BM3D, and TGV, respectively. These numerical results clearly indicate the high degree of accuracy and precision in CBF determination from images denoised using the NESMA-ASL filter as compared to conventional (*i.e.* BA and BG) or advanced filters.

Figure 2 shows CBF maps derived from CR ASL imaging datasets acquired from the brain of two participants before and after filtering using different filters described in the text. Results show substantial random variation in CBF maps derived from unfiltered images. This random variation was greatly decreased through filtering. However, CBF maps derived from images filtered with NESMA-ASL exhibited preservation of detail as well as greatly reduced random variation as compared to all evaluated filters; this is in good agreement with the numerical simulation analysis results.

Figure 3 shows CBF maps derived from CR or HR ASL imaging datasets acquired from the brain of the 61-year-old participant before and after filtering using the NESMA-ASL filter. Here again, the results show substantial random variation in CBF maps derived from unfiltered images. As expected, this variation was higher in CBF maps derived from HR as compared to those derived from CR ASL images due to lower SNR. In contrast, CBF maps derived from either CR or HR ASL images filtered with NESMA-ASL exhibited preservation of detail as well as greatly reduced random variation. Furthermore, while CR and HR CBF maps were generally similar, HR mapping allows greater depiction of the small-scale details of CBF distribution.

Figure 4 shows CBF maps derived from HR ASL imaging datasets acquired with different values of NSA from the brain of the 50-year-old participant. Results are shown for two different slices before and after filtering using NESMA-ASL. Visual inspection shows decreased random variation in CBF maps derived from unfiltered images with increasing NSA, that is, decreasing SNR, as expected. In contrast, CBF maps derived from NESMA-ASL filtered images were overall similar for different NSAs, especially for NSA > 3. Furthermore, quantitative analysis shows decrease in CBF mean and SD values calculated over large white or gray matter regions from unfiltered images with increasing NSA; this is due to the direct effect of reduced noise. In contrast, the CBF mean values derived from NESMA-ASL-filtered images were overall consistent over the whole range of NSA, except for a slightly larger value for the smallest NSA = 3. These results indicate the greatly improved consistency and insensitivity to SNR of NESMA-ASL-derived CBF maps.

Figure 5 shows a comparison of CBF maps derived from unfiltered or NESMA-ASL-filtered images from the CR datasets of the brains of the ten subjects, representing a wide agerange, for two imaging slices. Again, CBF maps derived from the NESMA-ASL-filtered images exhibited preservation of edges and small structures, as well as greatly reduced random variation as compared to those derived from unfiltered images. Moreover, both visual inspection (Fig. 5) and quantitative analysis (Fig. 6) indicate, overall, higher CBF values, derived from filtered or unfiltered ASL images, in the middle-aged subject as compared to values in the younger or the older subjects. This is seen in several white or gray matter brain regions including the frontal, temporal, parietal, and occipital lobes. Here again, the mean CBF values obtained from the unfiltered or filtered images were generally similar. However, the SD of CBF values derived from unfiltered images were larger than those derived from filtered images. In addition, our results indicate that using NESMA-ASL, it is possible to detect small changes in CBF, spanning a range of 5 to 20 ml/100g/min. This may be particularly important in relatively homogeneous white matter regions, where flow is substantially smaller than in gray matter. Finally, the quantitative results indicate overall

lower CBF mean values, obtained from the unfiltered or filtered images, in the GM regions lying within the partial lobes as compared to the other lobes.

4. DISCUSSION

Regional alterations in CBF have been found to be associated with brain development (Hagstadius and Risberg, 1989; Martin et al., 1991; Takahashi et al., 2005) and several central nervous system diseases, including dementia (Chao et al., 2010; Schuff et al., 2009), mild cognitive impairment (Luckhaus et al., 2008; Park et al., 2012), multiple sclerosis (Marshall et al., 2016; Ota et al., 2013), schizophrenia (Ota et al., 2014; Ragland et al., 2001), depression (Colloby et al., 2012; Wang et al., 2014), epilepsy (Appel et al., 2012; Touchon et al., 1986), and others (Alsop et al., 2000; Devet al., 2015; Du et al., 2006; Melzer et al., 2011). However, high-quality, HR MR imaging of CBF is challenging, especially in a clinical setting. In this study, we introduced a new application of the NESMA filter to improve determination of CBF from clinical ASL imaging data. Our analyses showed that estimation of CBF was markedly improved through use of the NESMA-ASL filter. Indeed, our results indicate that NESMA-ASL filtering results in CBF maps with increased anatomic detail and delineation of local CBF patterns as compared to results obtained from unfiltered images or filtered images using conventional or advanced filters. Moreover, the use of NESMA-ASL permits high-quality determination of CBF from ASL images obtained with HR or limited NSA. HR imaging permits greater depiction of details of the CBF distribution, while reduced NSA permits substantial reduction in the acquisition time.

A variety of filters have been used to improve CBF determination (Bibic et al., 2010; Spann et al., 2017; Wells et al., 2010). However, while effective, these filters require optimal selection of tuning parameters. For example, the TGV filter depends on model parameters which are sensitive to local image features and SNR (Bredies et al., 2010; Spann et al., 2017). Similarly, the AD filter is very sensitive to tuning parameters such as the diffusion step time, the conduction coefficient, and the number of iterations, with limited filtering performance (Spann et al., 2017; Wells et al., 2010) (Figs. 1-2). Further, the NLM filter requires careful selection of the smoothing parameter which is challenging in practice (Bouhrara et al., 2017a; Petr et al., 2010; Spann et al., 2017). Moreover, the wavelet-based Wiener filter requires optimization of the threshold factor which is challenging in actual practice, since the underlying pattern of image intensities is of course unknown (Bibic et al., 2010; Spann et al., 2017). These filters, as seen, while effective, can be extremely complex to implement and therefore are not likely to be adopted for routine clinical use. Advanced methods based on deep learning have been recently suggested for ASL image denoising(Kim et al., 2018; Ulas et al., 2018). While effective, these methods require advanced programing skills, large training datasets and computing power. In contrast, the NESMA-ASL filter is based on the established nonlocal filtering approach introduced by Buades *et al.* (Buades et al., 2005), and is a substantial simplification of the nonlocal maximum likelihood approach of He (He and Greenshields, 2009) and its multispectral extension presented by Bouhrara *et al.* (Bouhrara et al., 2017a). NESMA relies only on voxel selection followed by simple averaging and is distinct from other advanced ASL filters in that its implementation is virtually unsupervised. The filter is self- adaptive across image

regions with different levels of SNR and contrast. After establishing the appropriate neighborhood size, only one user-specified parameter, the RED cutoff threshold, must be specified, with results relatively insensitive to its exact value in the range of ~5%. The same threshold value was successfully used to improve myelin water fraction (MWF) mapping from MSE imaging datasets (Bouhrara et al., 2017b; Bouhrara et al., 2018b). Of note, as both *B1* and noise SD vary smoothly throughout the images (Aja-Fernández and Vegas-Sánchez-Ferrero, 2016; Bouhrara and Bonny, 2012; Bouhrara and Spencer, 2016; Rejimon et al., 2018), we found that a neighborhood of R = 15 mm x 15 mm x 15 mm provided excellent results through a range of spatial resolution, SNR, and CBF values.

In this work we analyzed two classes of filters: local and nonlocal. Depending upon the distribution of voxel intensities in the image, nonlocal filtering can greatly extend filtering capability by incorporating much more data into an intensity estimate. In addition, as shown by Buades (Buades et al., 2005) and subsequent investigators (Bouhrara et al., 2017a; He and Greenshields, 2009), nonlocal filters greatly lessen the tradeoff between resolution and noise reduction that is characteristic of local filters.

Our analysis showed CBF values consistent with the literature and demonstrate the sensitivity of the method to CBF changes with age (Chen et al., 2011; Parkes et al., 2004). However, our analysis was conducted on a very limited cohort; a larger group of subjects would be required for population-based regional comparisons. The present study indicates the utility of multispectral nonlocal filtering in undertaking such larger studies.

Our results showed a systematic overestimation in derived CBF values from unfiltered images at low SNR for both gray and white matter (Fig. 4b). We provisionally attribute this bias to the non-Gaussian noise distribution in the composite magnitude images. The noise in these images, obtained with multichannel coil acquisition and SENSE reconstruction, is expected to follow a noncentral χ-distribution (Bouhrara et al., 2015a; Bouhrara et al., 2015b; Bouhrara and Spencer, 2018). At low SNR, the noncentral χ-distribution deviates significantly from the Gaussian distribution (Bouhrara and Spencer, 2018) and exhibits a noise floor. However, this is not the case with filtered images, since the noncentral χ-distribution can be approximated by a Gaussian distribution at high SNR (Bouhrara and Spencer, 2018).

Studies investigating the relationship between perfusion and myelination in normative aging and neurodegeneration may provide insight into the processes underlying demyelination and its potential role in neurodegenerative diseases (Bouhrara et al., 2018a; Mustapha Bouhrara; David A. Reiter, 2017). Methods for high-quality HR myelin content mapping have recently been introduced (Bouhrara et al., 2018a; Bouhrara and Spencer, 2015; Bouhrara and Spencer; Bouhrara and Spencer, 2017; Mustapha Bouhrara; David A. Reiter, 2017). We believe that the use of NESMA-ASL for CBF mapping, in conjunction with high-quality MWF mapping, will permit voxel-wise statistical analyses to establish the potential association between myelin content and CBF. Finally, we observed lower CBF values in the parietal lobes; this is in good agreement with previous studies (Martin et al., 1991; Warach et al., 1992) and is likely due to the relative inactivity of the parietal lobes, known to be

modulated by sensation and perception, as compared to the other lobes during the resting state.

In this work, we applied NESMA-ASL to pCASL imaging datasets obtained from single-phase acquisition, that is, single PLD. This approach was based on the reasons put forward in the ASL ISMRM White Paper (Alsop et al., 2015) for recommending single-phase pCASL as a standard method in clinical practice. These include the relatively improved SNR in the pCASL acquired images as compared to pulsed ASL, the efficiency of blood labeling, the availability of the sequence in most MRI systems, and the simplicity of CBF quantification (Eq. 4). However, NESMA-ASL is, in principle, readily applicable to all ASL modalities for CBF determination, including multi-phase ASL acquisitions (Alsop et al., 2015; Qin et al., 2014). In this case, images obtained at different PLD would serve as multispectral images. In general, the NESMA algorithm is applicable to other quantitative modalities, in which successive images are obtained leading to multispectral characterization of individual voxels. One successful application has been to improve the determination of MWF from multi-spin-echoes (MSE) imaging data (Bouhrara et al., 2017b).

In conclusion, we performed CBF mapping in the human brain using a novel nonlocal filter. Although our analysis was performed on a limited cohort and a larger group of subjects would be required for population-based regional comparisons, we found that high resolution clinical mapping of CBF from ASL imaging data was markedly improved through use of the NESMA-ASL filter.

ACKNOWLEDGEMENTS

This work was supported by the Intramural Research Program of the NIH, National Institute on Aging.

REFERENCES

Aja-Fernández S, Vegas-Sánchez-Ferrero G. Statistical Analysis of Noise in MRI Springer International Publishing, 2016.

Alsop DC, Detre JA, Golay X, Gunther M, Hendrikse J, Hernandez-Garcia L, Lu H, MacIntosh BJ, Parkes LM, Smits M, van Osch MJ, Wang DJ, Wong EC, Zaharchuk G. Recommended implementation of arterial spin- labeled perfusion MRI for clinical applications: A consensus of the ISMRM perfusion study group and the European consortium for ASL in dementia. Magn Reson Med, 2015; 73: 102–16. [PubMed: 24715426]

Alsop DC, Detre JA, Grossman M. Assessment of cerebral blood flow in Alzheimer's disease by spin-labeled magnetic resonance imaging. Ann Neurol, 2000; 47: 93–100. [PubMed: 10632106]

Appel S, Duke ES, Martinez AR, Khan OI, Dustin IM, Reeves-Tyer P, Berl MB, Sato S, Gaillard WD, Theodore WH. Cerebral blood flow and fMRI BOLD auditory language activation in temporal lobe epilepsy. Epilepsia, 2012; 53: 631–8. [PubMed: 22332720]

Baskerville TA, McCabe C, Weir CJ, Macrae IM, Holmes WM. Noninvasive MRI measurement of CBF: evaluating an arterial spin labelling sequence with (99m)Tc-HMPAO CBF autoradiography in a rat stroke model. Journal of Cerebral Blood Flow & Metabolism, 2012; 32: 973–7. [PubMed: 22472604]

Bibic A, Knutsson L, Stahlberg F, Wirestam R. Denoising of arterial spin labeling data: wavelet-domain filtering compared with Gaussian smoothing. Magma (New York, N.Y.), 2010; 23: 125–37. [PubMed: 20424885]

Bouhrara M, Bonny JM. B(1) mapping with selective pulses. Magnetic resonance in medicine, 2012; 68: 1472–80. [PubMed: 22246956]

Bouhrara M, Bonny JM, Ashinsky BG, Maring MC, Spencer RG. Noise Estimation and Reduction in Magnetic Resonance Imaging Using a New Multispectral Nonlocal Maximum-likelihood Filter. IEEE transactions on medical imaging, 2017a; 36: 181–93. [PubMed: 27552743]

Bouhrara M, Maring CM, Reiter DA, Bonny JM, Spencer RG. Enhanced Quality of Myelin Water Fraction Mapping from GRASE Imaging Data of Human Brain using a New Nonlocal Estimation of multi-Spectral Magnitudes (NESMA) Filter ISMRM: Honolulu, HI, USA, 2017b.

Bouhrara M, Reiter DA, Bergeron CM, Zukley LM, Ferrucci L, Resnick SM, Spencer RG. Evidence of demyelination in mild cognitive impairment and dementia using a direct and specific magnetic resonance imaging measure of myelin content. Alzheimer's & Dementia, 2018a.

Bouhrara M, Reiter DA, Celik H, Bonny JM, Lukas V, Fishbein KW, Spencer RG. Incorporation of rician noise in the analysis of biexponential transverse relaxation in cartilage using a multiple gradient echo sequence at 3 and 7 tesla. Magnetic resonance in medicine, 2015a; 73: 352–66. [PubMed: 24677270]

Bouhrara M, Reiter DA, Maring MC, Bonny JM, Spencer RG. Use of the NESMA Filter to Improve Myelin Water Fraction Mapping with Brain MRI. Journal of neuroimaging : official journal of the American Society of Neuroimaging, 2018b.

Bouhrara M, Reiter DA, Spencer RG. Bayesian analysis of transverse signal decay with application to human brain. Magnetic resonance in medicine, 2015b; 74: 785–802. [PubMed: 25242062]

Bouhrara M, Spencer RG. Fisher information and Cramer-Rao lower bound for experimental design in parallel imaging. Magnetic resonance in medicine, 2018; 79: 3249–55. [PubMed: 29090485]

Bouhrara M, Spencer RG. Improved determination of the myelin water fraction in human brain using magnetic resonance imaging through Bayesian analysis of mcDESPOT. NeuroImage, 2016; 127: 456–71. [PubMed: 26499810]

Bouhrara M, Spencer RG. Incorporation of nonzero echo times in the SPGR and bSSFP signal models used in mcDESPOT. Magnetic resonance in medicine, 2015; 74: 1227–35. [PubMed: 26407635]

Bouhrara M, Spencer RG. Rapid Simultaneous High-resolution Mapping of Myelin Water Fraction and Relaxation Times in Human Brain using BMC-mcDESPOT. NeuroImage

Bouhrara M, Spencer RG. Rapid simultaneous high-resolution mapping of myelin water fraction and relaxation times in human brain using BMC-mcDESPOT. NeuroImage, 2017; 147: 800–11. [PubMed: 27729276]

Bredies K, Kunisch K, Pock T. Total Generalized Variation. SIAM J. Img. Sci, 2010; 3: 492–526.

Buades A, Coll B, Morel JM. A non-local algorithm for image denoising. 2005 IEEE Computer Society Conference on Computer Vision and Pattern Recognition (CVPR'05), 2005: 60–5 vol. 2.

Chao LL, Buckley ST, Kornak J, Schuff N, Madison C, Yaffe K, Miller BL, Kramer JH, Weiner MW. ASL perfusion MRI predicts cognitive decline and conversion from MCI to dementia. Alzheimer Dis Assoc Disord, 2010; 24: 19–27. [PubMed: 20220321]

Chen JJ, Rosas HD, Salat DH. Age-associated reductions in cerebral blood flow are independent from regional atrophy. Neuroimage, 2011; 55: 468–78. [PubMed: 21167947]

Colloby SJ, Firbank MJ, He J, Thomas AJ, Vasudev A, Parry SW, O'Brien JT. Regional cerebral blood flow in late-life depression: arterial spin labelling magnetic resonance study. Br J Psychiatry, 2012; 200: 150–5. [PubMed: 22194184]

Dabov K, Foi A, Katkovnik V, Egiazarian K. Image denoising by sparse 3-D transform-domain collaborative filtering. IEEE transactions on image processing : a publication of the IEEE Signal Processing Society, 2007; 16: 2080–95. [PubMed: 17688213]

Dev SI, McKenna BS, Sutherland AN, Shin DD, Liu TT, Wierenga CE, Eyler LT. Increased cerebral blood flow associated with better response inhibition in bipolar disorder. J Int Neuropsychol Soc, 2015; 21: 105–15. [PubMed: 25771682]

Du AT, Jahng GH, Hayasaka S, Kramer JH, Rosen HJ, Gorno-Tempini ML, Rankin KP, Miller BL, Weiner MW, Schuff N. Hypoperfusion in frontotemporal dementia and Alzheimer disease by arterial spin labeling MRI. Neurology, 2006; 67: 1215–20. [PubMed: 17030755]

Gerig G, Kubler O, Kikinis R, Jolesz FA. Nonlinear anisotropic filtering of MRI data. IEEE transactions on medical imaging, 1992; 11: 221–32. [PubMed: 18218376]

Hagstadius S, Risberg J. Regional cerebral blood flow characteristics and variations with age in resting normal subjects. Brain Cogn, 1989; 10: 28–43. [PubMed: 2713143]

He L, Greenshields IR. A Nonlocal Maximum Likelihood Estimation Method for Rician Noise Reduction in MR Images. IEEE transactions on medical imaging, 2009; 28: 165–72. [PubMed: 19188105]

Jin F, Fieguth P, Winger L, Jernigan E. Adaptive Wiener filtering of noisy images and image sequences. Proceedings 2003 International Conference on Image Processing (Cat. No. 03CH37429), 2003: III-349–52 vol.2.

Kim KH, Choi SH, Park S-H. Improving Arterial Spin Labeling by Using Deep Learning. Radiology, 2018; 287: 658–66. [PubMed: 29267145]

Liang X, Connelly A, Calamante F. Voxel-Wise Functional Connectomics Using Arterial Spin Labeling Functional Magnetic Resonance Imaging: The Role of Denoising. Brain connectivity, 2015; 5: 543–53. [PubMed: 26020288]

Luckhaus C, Fluss MO, Wittsack HJ, Grass-Kapanke B, Janner M, Khalili-Amiri R, Friedrich W, Supprian T, Gaebel W, Modder U, Cohnen M. Detection of changed regional cerebral blood flow in mild cognitive impairment and early Alzheimer's dementia by perfusion-weighted magnetic resonance imaging. Neuroimage, 2008; 40: 495–503. [PubMed: 18207425]

Maring MC, Bouhrara M, Spencer RG. A Fast Adaptive Multispectral Nonlocal Denoising Filter ISMRM: Honolulu, HI, USA, 2017.

Marshall O, Chawla S, Lu H, Pape L, Ge Y. Cerebral blood flow modulation insufficiency in brain networks in multiple sclerosis: A hypercapnia MRI study. J Cereb Blood Flow Metab, 2016; 36: 2087–95. [PubMed: 27306754]

Martin AJ, Friston KJ, Colebatch JG, Frackowiak RS. Decreases in regional cerebral blood flow with normal aging. J Cereb Blood Flow Metab, 1991; 11: 684–9. [PubMed: 2050757]

Melzer TR, Watts R, MacAskill MR, Pearson JF, Rueger S, Pitcher TL, Livingston L, Graham C, Keenan R, Shankaranarayanan A, Alsop DC, Dalrymple-Alford JC, Anderson TJ. Arterial spin labelling reveals an abnormal cerebral perfusion pattern in Parkinson's disease. Brain, 2011; 134: 845–55. [PubMed: 21310726]

Bouhrara Mustapha; Reiter CMB David A., Zukley Linda M., Resnick Susan M., Studenski Stephanie, Egan Josephine M., Ferrucci Luigi, and Spencer Richard G.. Demyelination in Mild Cognitive Impairment ISMRM: Honolulu, HI, USA, 2017.

Ota M, Ishikawa M, Sato N, Okazaki M, Maikusa N, Hori H, Hattori K, Teraishi T, Ito K, Kunugi H. Pseudo- continuous arterial spin labeling MRI study of schizophrenic patients. Schizophr Res, 2014; 154: 113–8. [PubMed: 24581548]

Ota M, Sato N, Nakata Y, Ito K, Kamiya K, Maikusa N, Ogawa M, Okamoto T, Obu S, Noda T, Araki M, Yamamura T, Kunugi H. Abnormalities of cerebral blood flow in multiple sclerosis: a pseudocontinuous arterial spin labeling MRI study. Magn Reson Imaging, 2013; 31: 990–5. [PubMed: 23582984]

Park KW, Yoon HJ, Kang DY, Kim BC, Kim S, Kim JW. Regional cerebral blood flow differences in patients with mild cognitive impairment between those who did and did not develop Alzheimer's disease. Psychiatry Res, 2012; 203: 201–6. [PubMed: 22980226]

Parkes LM, Rashid W, Chard DT, Tofts PS. Normal cerebral perfusion measurements using arterial spin labeling: Reproducibility, stability, and age and gender effects. Magnetic Resonance in Medicine, 2004; 51: 736–43. [PubMed: 15065246]

Perona P, Malik J. Scale-space and edge detection using anisotropic diffusion. IEEE Transactions on Pattern Analysis and Machine Intelligence, 1990; 12: 629–39.

Petcharunpaisan S, Ramalho J, Castillo M. Arterial spin labeling in neuroimaging. World Journal of Radiology, 2010; 2: 384–98. [PubMed: 21161024]

Petr J, Ferre J-C, Gauvrit J-Y, Barillot C. Improving arterial spin labeling data by temporal filtering. SPIE Medical Imaging SPIE, 2010: 9.

Pollock JM, Tan H, Kraft RA, Whitlow CT, Burdette JH, Maldjian JA. Arterial spin-labeled MR perfusion imaging: clinical applications. Magn Reson Imaging Clin N Am, 2009; 17: 315–38. [PubMed: 19406361]

Qin Q, Huang AJ, Hua J, Desmond JE, Stevens RD, van Zijl PCM. Three-dimensional whole-brain perfusion quantification using pseudo-continuous arterial spin labeling MRI at multiple post-

labeling delays: accounting for both arterial transit time and impulse response function. NMR in biomedicine, 2014; 27: 116–28. [PubMed: 24307572]

Ragland JD, Gur RC, Raz J, Schroeder L, Kohler CG, Smith RJ, Alavi A, Gur RE. Effect of schizophrenia on frontotemporal activity during word encoding and recognition: a PET cerebral blood flow study. Am J Psychiatry, 2001; 158: 1114–25. [PubMed: 11431234]

Rejimon AC, Lee DY, Bergeron CM, Zhuo Y, Qian W, Spencer RG, Bouhrara M. Rapid B1 field mapping at 3T using the 180 degrees signal null method with extended flip angle. Magnetic resonance imaging, 2018.

Schuff N, Matsumoto S, Kmiecik J, Studholme C, Du AT, Ezekiel F, Miller BL, Kramer JH, Jagust WJ, Chui HC, Weiner MW. Cerebral blood flow in ischemic vascular dementia and Alzheimer's disease, measured by arterial spin-labeling magnetic resonance imaging. Alzheimers & Dementia, 2009; 5: 454–62.

Spann SM, Kazimierski KS, Aigner CS, Kraiger M, Bredies K, Stollberger R. Spatio-temporal TGV denoising for ASL perfusion imaging. NeuroImage, 2017; 157: 81–96. [PubMed: 28559192]

Takahashi K, Yamaguchi S, Kobayashi S, Yamamoto Y. Effects of aging on regional cerebral blood flow assessed by using technetium Tc 99m hexamethylpropyleneamine oxime single-photon emission tomography with 3D stereotactic surface projection analysis. Am J Neuroradiol, 2005; 26: 2005–9. [PubMed: 16155150]

Tan H, Maldjian JA, Pollock JM, Burdette JH, Yang LY, Deibler AR, Kraft RA. A fast, effective filtering method for improving clinical pulsed arterial spin labeling MRI. J Magn Reson Imaging, 2009; 29: 1134–9. [PubMed: 19388118]

Touchon J, Valmier J, Baldy-Moulinier M, Cadilhac J. Regional cerebral blood flow during interictal state: differences between temporal lobe epilepsy and primary generalized epilepsy. Eur Neurol, 1986; 25: 43– 52. [PubMed: 3940865]

Ulas C, Tetteh G, Kaczmarz S, Preibisch C, Menze BH. DeepASL: Kinetic Model Incorporated Loss for Denoising Arterial Spin Labeled MRI via Deep Residual Learning. ArXiv e-prints, 2018.

Wang YM, Zhang HM, Tang SL, Liu XD, O'Neil A, Turner A, Chai FX, Chen FY, Berk M. Assessing Regional Cerebral Blood Flow in Depression Using 320-Slice Computed Tomography. Plos One, 2014; 9.

Warach S, Gur RC, Gur RE, Skolnick BE, Obrist WD, Reivich M. Decreases in frontal and parietal lobe regional cerebral blood flow related to habituation. J Cereb Blood Flow Metab, 1992; 12: 546–53. [PubMed: 1618933]

Wells JA, Thomas DL, King MD, Connelly A, Lythgoe MF, Calamante F. Reduction of errors in ASL cerebral perfusion and arterial transit time maps using image de-noising. Magnetic resonance in medicine, 2010; 64: 715–24. [PubMed: 20578044]

Williams DS, Detre JA, Leigh JS, Koretsky AP. Magnetic resonance imaging of perfusion using spin inversion of arterial water. Proc Natl Acad Sci U S A, 1992; 89: 212–6. [PubMed: 1729691]

Zhao MY, Mezue M, Segerdahl AR, Okell TW, Tracey I, Xiao Y, Chappell MA. A systematic study of the sensitivity of partial volume correction methods for the quantification of perfusion from pseudo- continuous arterial spin labeling MRI. NeuroImage, 2017; 162: 384–97. [PubMed: 28887087]

Zhu H, Zhang J, Wang Z. Arterial spin labeling perfusion MRI signal denoising using robust principal component analysis. Journal of Neuroscience Methods, 2018; 295: 10–9. [PubMed: 29196191]

Highlights

- We applied the NESMA filter to improve cerebral blood flow (CBF) mapping from ASL MRI data
- The NESMA-ASL filter outperforms other advanced filters in terms of noise reduction and detail preservation
- NESMA-ASL is spatially adaptive, requires only one user-defined parameter, and is straightforward to implement

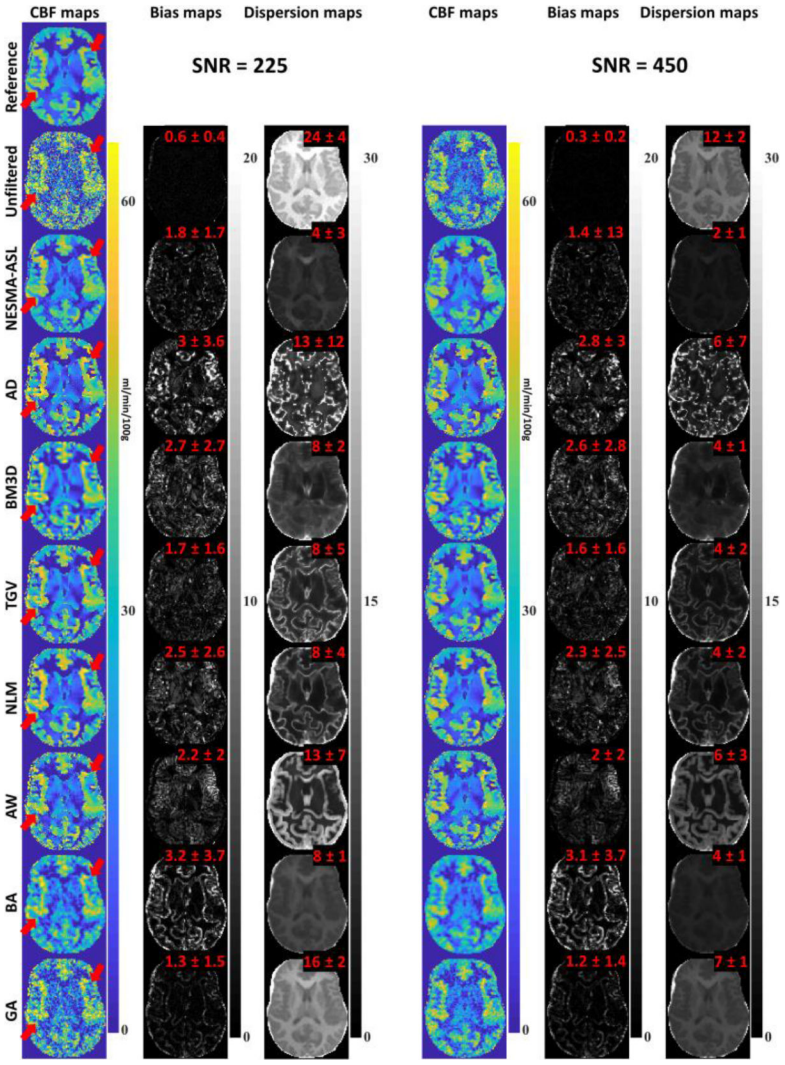

Figure 1.

Simulated cerebral blood flow (CBF) maps derived from arterial spin labeling imaging datasets, generated at two SNRs, before and after filtering using the filters described in the text. For each filter and SNR, the corresponding bias, a measure of accuracy, and dispersion, a measure of precision, maps were calculated on a voxel-by-voxel basis and are displayed. Furthermore, mean and SD bias and dispersion values calculated over all parenchymal regions are also displayed. The NESMA-ASL filters show, overall, higher denoising performance as compared to the other filters. Red arrows indicate example of regions where NESMA-ASL shows higher performance and preservation of detail. [Color image]

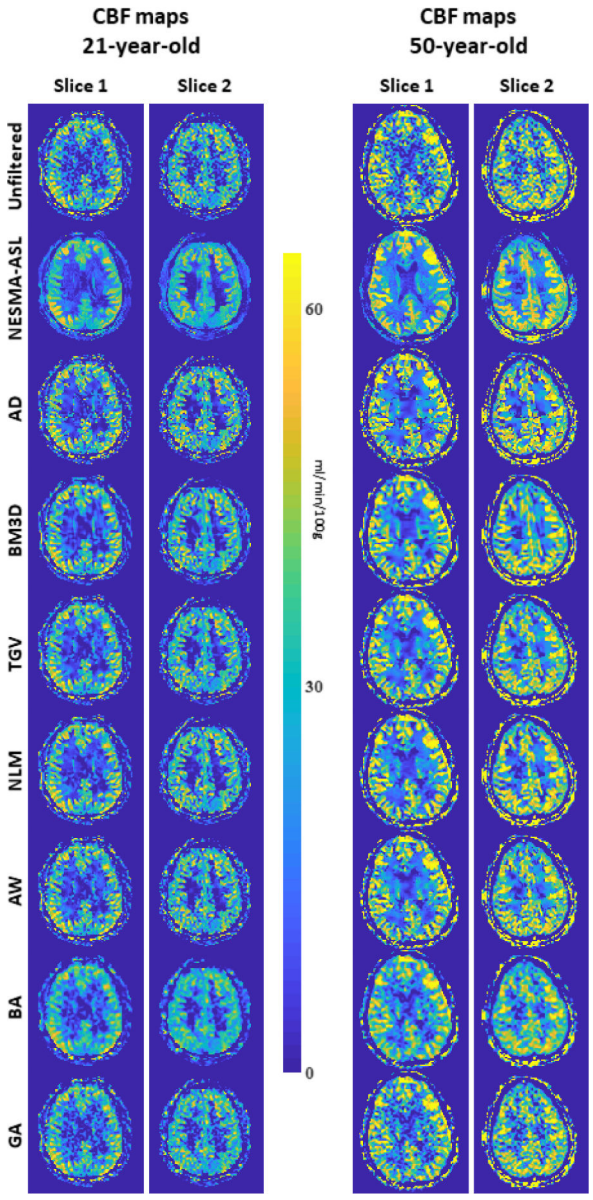

Figure 2.

In-vivo results. Cerebral blood flow (CBF) maps derived from two arterial spin labeling imaging datasets, obtained from the brain of the 21-year-old and 50-year-old participants with NSA = 30, before and after filtering using the different filters described in the text. For each filter and participant, two representative CBF maps corresponding to different slice locations were displayed. The NESMA-ASL filters show, overall, higher denoising performance with greater preservation of details as compared to all evaluated filters. [Color image]

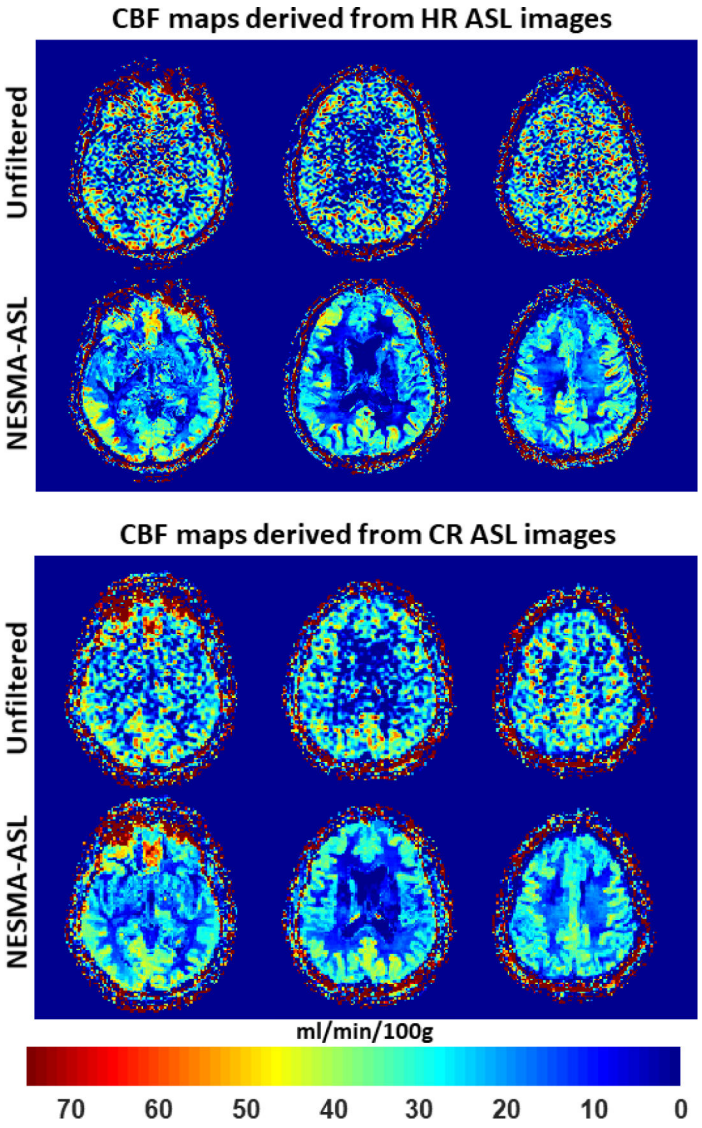

Figure 3.

In-vivo results. Cerebral blood flow (CBF) maps derived from high-resolution (HR) or conventional-resolution (CR) arterial spin labeling (ASL) imaging datasets acquired from the brain of the 61-year-old with NSA = 30 participant before and after filtering using the NESMA- ASL filter. Results are shown for three different slices. [Color image]

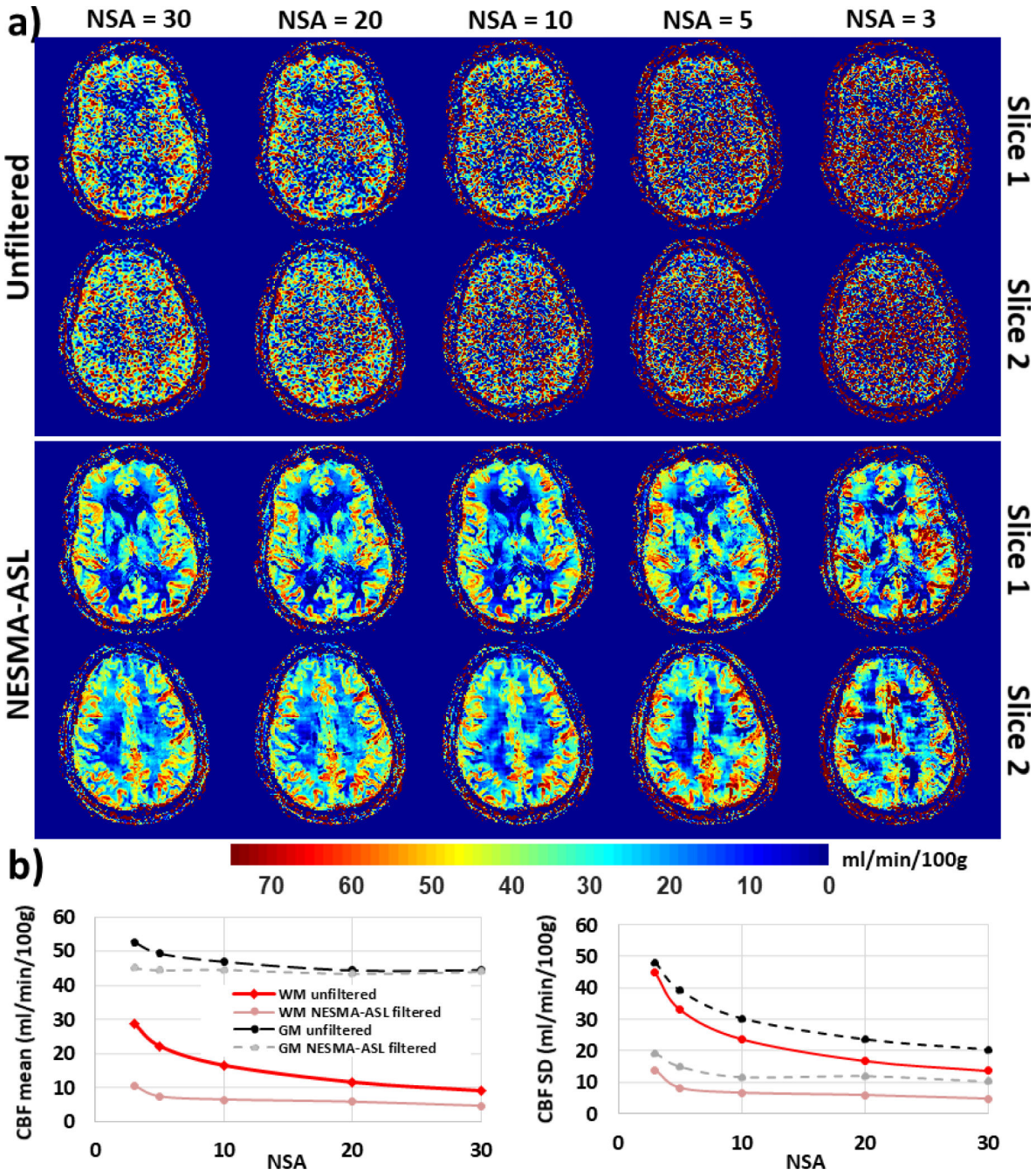

Figure 4.

In-vivo results. a) Cerebral blood flow (CBF) maps derived from high-resolution arterial spin labeling (ASL) imaging datasets acquired with different degrees of signal averaging (NSA) from the brain of the 50-year-old participant. Results are shown before and after filtering using NESMA-ASL for two different slices. b) Mean and standard deviation (SD) CBF values calculated over large white matter (WM) or gray matter (GM) regions as a function of NSA from unfiltered or NESMA-ASL-filtered images. [Color image]

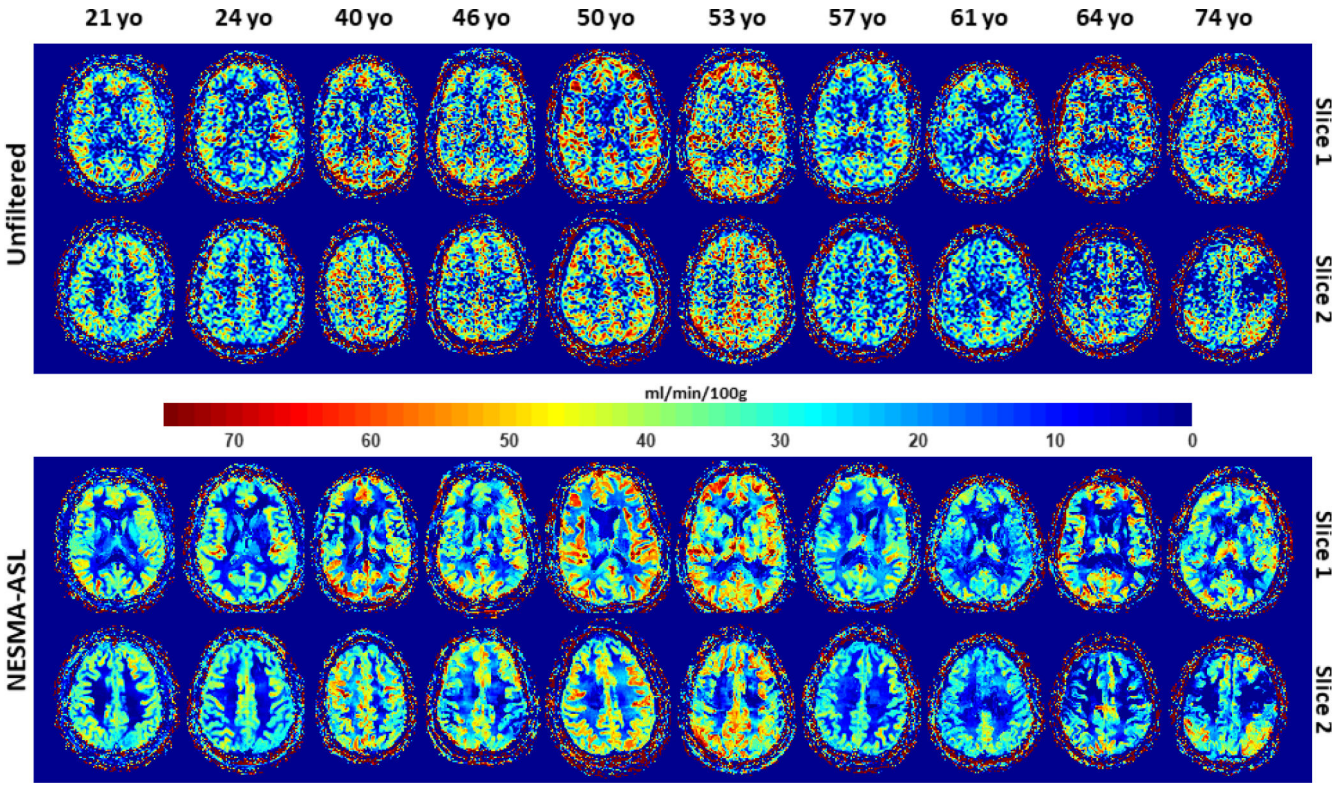

Figure 5.

In-vivo results. Cerebral blood flow (CBF) maps derived from low-resolution arterial spin labeling (ASL) imaging datasets acquired from the brains of ten participants of different ages with NSA = 30. For each participant, CBF maps are shown for two representative slices. [Color image]

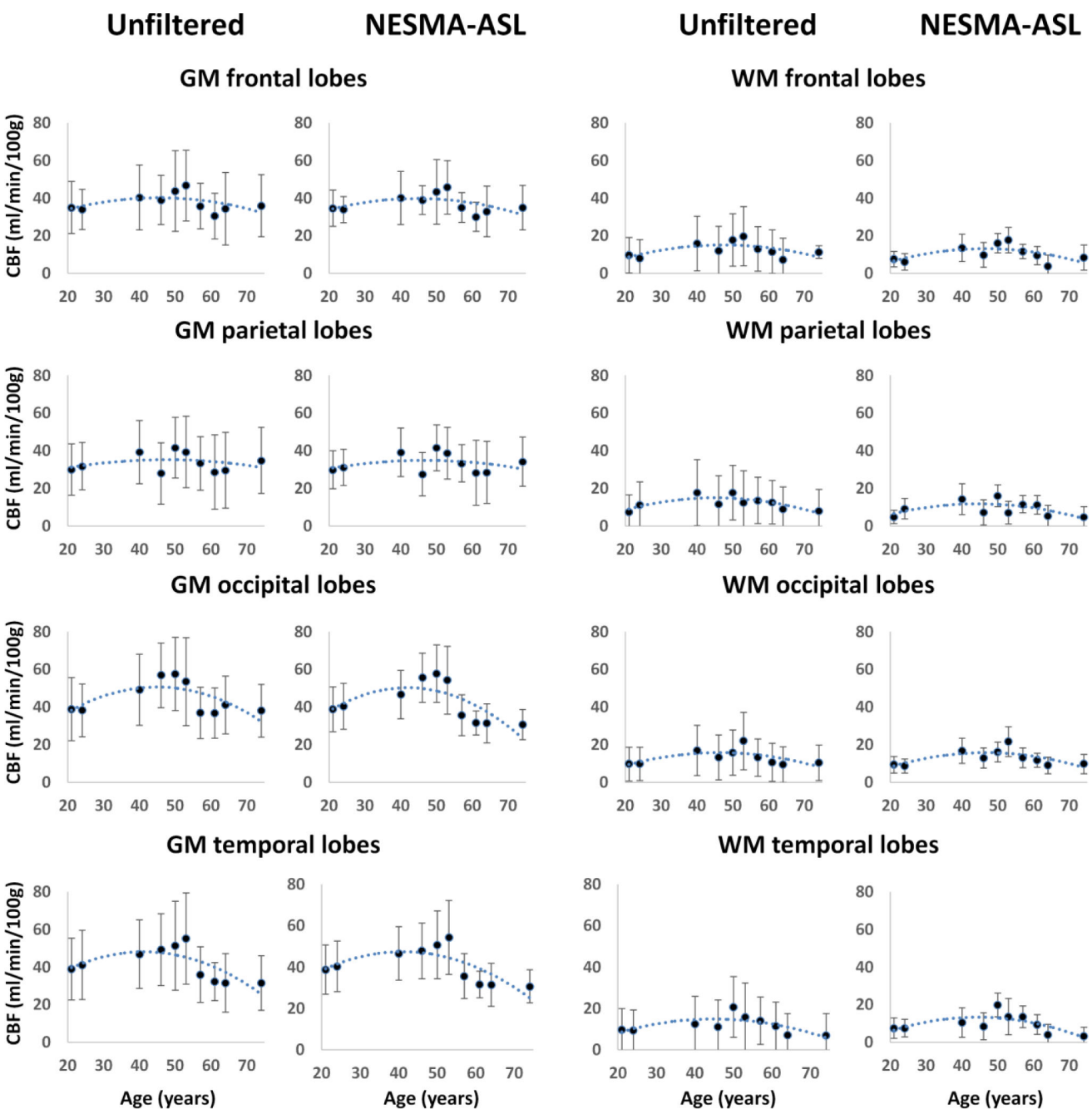

Figure 6.

Mean and standard deviation of cerebral blood flow (CBF) values calculated from unfiltered or NESMA-ASL filtered images in different gray matter (GM) or white matter (WM) regions within the frontal, parietal, occipital and temporal lobes. Dotted trendlines were obtained through a second order polynomial regression.

Table 1.

Participants information.

	Age (years)	Sex	CR images	HR images
Participant #1	21	Male	Yes	No
Participant #2	24	Male	Yes	Yes
Participant #3	40	Female	Yes	No
Participant #4	46	Male	Yes	No
Participant #5	50	Male	Yes	Yes
Participant #6	53	Male	Yes	No
Participant #7	57	Female	Yes	Yes
Participant #8	61	Female	Yes	Yes
Participant #9	64	Female	Yes	No
Participant #10	74	Male	Yes	No